

# Reconstruction of Cloud Vertical Structure with a Generative Adversarial Network

Jussi Leinonen<sup>1,2</sup>, Alexandre Guillaume<sup>1</sup>, Tianle Yuan<sup>3,4</sup>

<sup>1</sup>Jet Propulsion Laboratory, California Institute of Technology, Pasadena, California, USA

<sup>2</sup>Environmental Remote Sensing Laboratory, École Polytechnique Fédérale de Lausanne, Lausanne,  
Switzerland

<sup>3</sup>Joint Center for Earth Systems Technology, University of Maryland, Baltimore County, Catonsville,  
Maryland, USA

<sup>4</sup>Earth Sciences Division, NASA Goddard Space Flight Center, Greenbelt, Maryland, USA

## Key Points:

- We trained a generative adversarial network (GAN) to generate cloud vertical structures.
- The network generates plausible CloudSat scenes, given MODIS data as an input.
- This demonstrates the potential usefulness of GANs in atmospheric science.

---

Corresponding author: Jussi Leinonen, [jussi.leinonen@epfl.ch](mailto:jussi.leinonen@epfl.ch)

## Abstract

We demonstrate the feasibility of solving atmospheric remote sensing problems with machine learning using conditional generative adversarial networks (CGANs), implemented using convolutional neural networks (CNNs). We apply the CGAN to generating two-dimensional cloud vertical structures that would be observed by the CloudSat satellite-based radar, using only the collocated Moderate-Resolution Imaging Spectrometer (MODIS) measurements as input. The CGAN is usually able to generate reasonable guesses of the cloud structure, and can infer complex structures such as multilayer clouds from the MODIS data. This network, which is formulated probabilistically, also estimates the uncertainty of its own predictions. We examine the statistics of the generated data, and analyze the response of the network to each input parameter. The success of the CGAN in solving this problem suggests that generative adversarial networks are applicable to a wide range of problems in atmospheric science, a field characterized by complex spatial structures and observational uncertainties.

## 1 Introduction

Clouds are a major component of the hydrological cycle of the Earth and greatly affect its radiative balance, constituting one of the most important yet least well understood climate feedbacks (e.g. Stevens & Bony, 2013; Vial, Dufresne, & Bony, 2013). Since the radiative effect of clouds is greatly dependent on their altitude (Stephens, 2005), their vertical distribution must be understood in order to fully observationally constrain their climate impact. While dozens of passive satellite sensors are currently operational, providing continuous monitoring of clouds in all regions of the Earth, they mostly measure the cloud top height, often in a biased manner (e.g. Garay, de Szoeke, & Moroney, 2008; Marchand, Ackerman, Smyth, & Rossow, 2010), and thus are unable to fully characterize the vertical profile. Active cloud-observing instruments, i.e. radars and lidars, can resolve the cloud vertical structure, but their coverage is much more sparse, with only a few such instruments currently operational in Earth orbit. The large disparity in spatial coverage is one reason for the lack of a global three-dimensional (3D) cloud observations dataset. This absence is a major limitation in the development and validation of atmospheric models. Moreover, the observations of passive sensors are themselves affected by the three-dimensional cloud structure, which can affect the radiative transfer in a manner that is inconsistent with the assumptions of the retrieval algorithms used to derive the physical properties of the cloud (Várnai & Marshak, 2002).

To mitigate the large disparity between passive and active sensor spatial coverage, different computational or algorithm approaches are available. For instance, several algorithms have been proposed to construct 3D cloud fields using data from both kinds of sensors as input (Barker et al., 2011; Ham, Kato, Barker, Rose, & Sun-Mack, 2015), thereby enabling simulation of solar radiative transfer from available data. However, the Barker et al. (2011) algorithm constructs each vertical column in the 3D cloud field from a nearby column with similar radiances. While this approach seems successful near the measured cross section, and suffices for modeling radiative properties, it would likely not create completely geometrically realistic 3D clouds, as each column in the 3D field is simply a copy of one of the measured columns.

Neural networks have recently greatly improved in capability to adapt to data with complex spatial structures, owing particularly to the introduction of convolutional neural networks (CNNs; e.g. Krizhevsky, Sutskever, & Hinton, 2012; LeCun, Bengio, & Hinton, 2015), as well as improved optimization and normalization algorithms that have enabled the training of deeper networks. Furthermore, improvements in generative models, which characterize the probability distribution of the training data, have been recently driven particularly by the invention of generative adversarial networks (GANs; Goodfellow et al., 2014; Radford, Metz, & Chintala, 2015, see also Sect. 3). These use

66 adversarial training to learn to map a simple probability distribution (e.g. a set of in-  
 67 dependent standard normal variables) to the training data distribution. GANs can learn  
 68 to generate artificial samples that strongly resemble those found in the training set. A  
 69 relatively straightforward variant, the conditional GAN (CGAN; Mirza & Osindero, 2014),  
 70 learns the distribution conditional to a given input. CGANs can learn to solve condi-  
 71 tional probability problems in which the random fields have complex spatial structures,  
 72 and thus are directly applicable to cloud vertical profile reconstruction. Since GANs learn  
 73 directly from the data, they allow for solutions that might be precluded by algorithms  
 74 using prescribed rules.

75 In this paper, we introduce the application of CGANs to probabilistic problem solv-  
 76 ing in atmospheric remote sensing. We demonstrate the concept by generating Cloud-  
 77 Sat radar scenes from collocated Moderate-Resolution Imaging Spectroradiometer (MODIS)  
 78 observations. Thus, we solve a sub-problem of the 3D reconstruction problem stated above  
 79 by reconstructing two-dimensional (2D) cloud vertical structures from one-dimensional  
 80 (1D) MODIS data.

## 81 2 Data

82 The CloudSat satellite (Stephens et al., 2008) carries a nadir-looking 94 GHz cloud  
 83 radar, located in the A-Train constellation at a 705 km sun-synchronous orbit. The pri-  
 84 mary data product is the radar reflectivity, given in the logarithmic dBZ units, which  
 85 is available in the 2B-GEOPROF data product (Marchand, Mace, Ackerman, & Stephens,  
 86 2008). The MODIS spectrometer (Platnick et al., 2003) on the Aqua satellite is also part  
 87 of the A-Train constellation, in which CloudSat operated for the majority of its mission,  
 88 allowing close spatiotemporal collocation of the data from the two instruments. The Aqua  
 89 MODIS data have been mapped to the CloudSat data coordinates in the CloudSat MOD06-  
 90 AUX product.

91 We used the entire year 2010 of the 2B-GEOPROF and MOD06-AUX products as  
 92 the basis of our dataset. From these data, we extracted non-overlapping rectangular patches  
 93 of radar reflectivity,  $64 \times 64$  radar bins in size. We refer to these as “scenes” through-  
 94 out this paper. In physical coordinates, the  $64 \times 64$  size corresponds to approximately  
 95 15 km in height and 70 km in horizontal along-track distance, owing to the 1.1 km along-  
 96 track resolution and 240 m vertical bin size of CloudSat. The scene height is sufficient  
 97 to cover nearly the entire altitude range where CloudSat is able to detect clouds, while  
 98 the horizontal extent means that the scenes reflect mesoscale organization of clouds and  
 99 precipitation. We chose this approach, rather than processing each column individually,  
 100 because adjacent columns are often similar, and thus their probability distributions are  
 101 strongly dependent on each other. Furthermore, the 70 km scale represents a good com-  
 102 promise between how statistically representative it is of observed cloud scales, and how  
 103 much it includes horizontal cloud correlations. Guillaume et al. (2018) have shown that  
 104 the distribution of horizontal cloud chord length evaluated from CloudSat data was heav-  
 105 ily skewed towards short scales, so that clouds at the CloudSat horizontal resolution of  
 106 1.1 km are vastly more frequent than clouds at scales of about 2000 km, which are very  
 107 rare.

108 From the MOD06-AUX product, we extracted four variables: cloud top pressure  
 109 ( $P_{\text{top}}$ ), cloud optical depth ( $\tau_c$ ), effective radius ( $r_e$ ) and cloud water path (CWP). Ad-  
 110 ditionally, we generated a binary cloud mask variable to indicate whether a cloud was  
 111 detected by MODIS in a given column (if not, this might be either because a cloud was  
 112 actually absent, or due to missing data). Thus, the MODIS data consists of five 64-bin  
 113 time series for each scene.

114 In preprocessing, we rescaled the CloudSat radar reflectivity  $Z_{\text{dB}}$  linearly from the  
 115 range  $[-35 \text{ dBZ}, 20 \text{ dBZ}]$  to  $[-1, 1]$  as

$$Z'_{\text{dB}} = 2 \frac{Z_{\text{dB}} + 35 \text{ dB}}{55 \text{ dB}} - 1, \quad (1)$$

116 with missing points and bins below  $-35 \text{ dBZ}$  set to  $-1$ , and bins above  $20 \text{ dBZ}$  set to  
 117  $1$ . We mapped the missing values to the minimum values because radar reflectivity tends  
 118 to decrease on the edges of clouds and precipitating regions, and thus this allows a smooth  
 119 transition between cloudy and cloudless regions. The MODIS variables (except the cloud  
 120 mask) were rescaled as follows:

$$121 \quad P'_{\text{top}} = (P_{\text{top}} - 532 \text{ hPa})/265 \quad (2)$$

$$122 \quad \tau'_c = (\ln \tau_c - 2.20)/1.13 \quad (3)$$

$$123 \quad r'_e = (\ln(r_e/(1 \mu\text{m})) - 3.06)/0.542 \quad (4)$$

$$124 \quad CWP' = (\ln(CWP/(1 \text{ g m}^{-2})) - 0.184)/1.11. \quad (5)$$

125 These transformations scale the variables in the dataset near to zero mean and unit vari-  
 126 ance; the logarithm transform was used for some variables to reduce skew. The missing  
 127 values for these variables were treated differently from the radar reflectivity because not  
 128 all of them tend to 0 near the cloud edges. Instead, we set each transformed variable to  
 129 0 where the data was missing, and also set the cloud mask to 0, as opposed to a mask  
 130 of 1 where data was available. This provides information to the network regarding the  
 131 location of the missing values, helping the network learn to distinguish between cloudy  
 132 and cloud-free areas.

133 The scenes are limited to daytime observations because some MODIS variables are  
 134 based on measurements of sunlight scattering from the cloud, and thus are not available  
 135 at night. To avoid complications due to terrain echoes in the radar data, we also lim-  
 136 ited the scenes to those occurring over the oceans. Finally, to avoid processing large num-  
 137 bers of near-empty scenes, we limited the dataset to scenes where the MODIS cloud mask  
 138 indicated a cloud in at least 50% of bins. We recognize that this downselection, made  
 139 in the interest of efficiency, introduces some bias into the global distribution of samples.  
 140 The same applies to the use of a single year of training data, which neglects possible in-  
 141 terannual variability in the modeled relationship of MODIS-derived cloud properties and  
 142 radar reflectivity. Depending on the application, it might be useful to retrain the model  
 143 with different selection criteria.

144 The final dataset consists of 199622 scenes. Of these, 90% were selected randomly  
 145 for training, while the remaining 10% were set aside for validation.

146 The output of the generator network is scaled back to  $[-35 \text{ dBZ}, 20 \text{ dBZ}]$ . Output  
 147 bins that have a reflectivity lower than  $-30 \text{ dBZ}$  are then flagged as missing values. This  
 148 is done because CloudSat rarely detects signals below  $-30 \text{ dBZ}$ , and because the net-  
 149 work sometimes generates weak spurious outputs at just above the minimum value. This  
 150 postprocessing removes these artifacts effectively, thus improving the visual similarity  
 151 of the real and generated images.

### 152 3 GAN architecture and training

153 The machine learning problem is stated formally as follows: Given a vector  $\mathbf{y}$ , con-  
 154 taining the MODIS observations described above, we seek to characterize the conditional  
 155 probability distribution  $p_{\text{data}}(\mathbf{x}|\mathbf{y})$  of CloudSat scenes  $\mathbf{x}$ . We use the CGAN to solve this  
 156 problem by training a *generator* neural network to map vectors  $\mathbf{z}$ , whose each element  
 157  $z_i$  is sampled from the standard normal distribution, to CloudSat scenes  $\mathbf{x}$ , conditional  
 158 to the MODIS observation vectors  $\mathbf{y}$ . Following the GAN principle, the generator is trained  
 159 adversarially against a *discriminator* network, which is trained simultaneously with the

160 generator. The discriminator is trained to distinguish generated samples from real sam-  
 161 ples, while the generator is trained to “fool” the discriminator as much as possible.

162 For the generator, we use a deep convolutional neural network that takes as its in-  
 163 puts the MODIS observation vector  $\mathbf{y}$  and the noise vector  $\mathbf{z}$ . The generator has one densely  
 164 connected layer followed by four convolutional layers. Following the deep convolutional  
 165 GAN (Radford et al., 2015) practices, we use upsampling layers followed by convolution.  
 166 Each hidden layer is followed by a rectified linear unit (ReLU) activation (Nair & Hin-  
 167 ton, 2010) and a batch normalization step (Ioffe & Szegedy, 2015). The final layer uses  
 168 a tanh activation with outputs between  $-1$  and  $1$ ; this is then rescaled to the appropri-  
 169 ate dBZ range.

170 The discriminator takes as its input an scene  $\mathbf{x}$  and a MODIS observation vector  
 171  $\mathbf{y}$ . The MODIS observations are first upsampled into  $64 \times 64$  bin channels using a four-  
 172 layer convolutional network similar to the architecture used in the generator. The up-  
 173 sampled MODIS observations and the generated image are then processed using four hid-  
 174 den layers, each using strided convolutions followed by leaky ReLU activations (with neg-  
 175 ative slope of 0.2) and dropout. The output layer is densely connected to the final hid-  
 176 den layer, and is sigmoid-activated to yield a number between 0 and 1 representing the  
 177 probability that the input scene is a fake sample created by the generator (as opposed  
 178 to a real CloudSat scene).

179 The generator and discriminator networks are described in detail in Fig. S1 of the  
 180 supporting information. The code and training data are available as described in the Ac-  
 181 knowledgments.

182 To train the CGAN, we alternated between training the generator with a single batch  
 183 of data and training the discriminator with two batches, one containing real samples and  
 184 the other containing generated samples. We train the CGAN for a total of 45 epochs,  
 185 gradually increasing the training batch size from 32 to 256. The Adam optimizer (Kingma  
 186 & Ba, 2014) was used to train both the generator and the discriminator. We performed  
 187 the training using a single Nvidia Tesla K80 general-purpose graphics processing unit;  
 188 the full training required approximately 40 hours.

## 189 4 Results

### 190 4.1 Generated vs. real scenes

191 Figure 1 displays selected examples of generated CloudSat scenes for a variety of  
 192 different MODIS measurements. The top two rows in each column show the MODIS vari-  
 193 ables, the four middle rows show scenes generated by the CGAN from the MODIS data,  
 194 and the bottom row shows the actual CloudSat scene that corresponds to the MODIS  
 195 data. All data shown are from the validation dataset, that is, they were not used to train  
 196 the network. Of the generated scenes, the topmost shows the image generated with the  
 197 noise input  $\mathbf{z}$  set to all zeros, representing the most likely answer according to the CGAN.  
 198 The other generated images were created with randomly sampled noise vectors. On each  
 199 generated image, a root-mean-square error (RMSE) relative to the real image is also plot-  
 200 ted, calculated such that missing data were set to  $-30$  dBZ before taking the difference.  
 201 The RMSE is an imperfect metric because the GAN is explicitly not designed to opti-  
 202 mize the RMSE, but rather the visual similarity, as defined by the discriminator. In gen-  
 203 eral, quantitative evaluation of GAN-generated images is a topic of ongoing debate with  
 204 no clear consensus (Borji, 2018). Nevertheless, the RMSE can give some indication of  
 205 the accuracy of the reconstruction.

206 It is evident from Fig. 1 that the CGAN generator can create realistic-looking radar  
 207 reflectivity scenes. Columns 1–2 show scenes that contain fairly uniform cloud layers.  
 208 In these, the structure of the cloud is accurately predicted by the CGAN: The radar echo

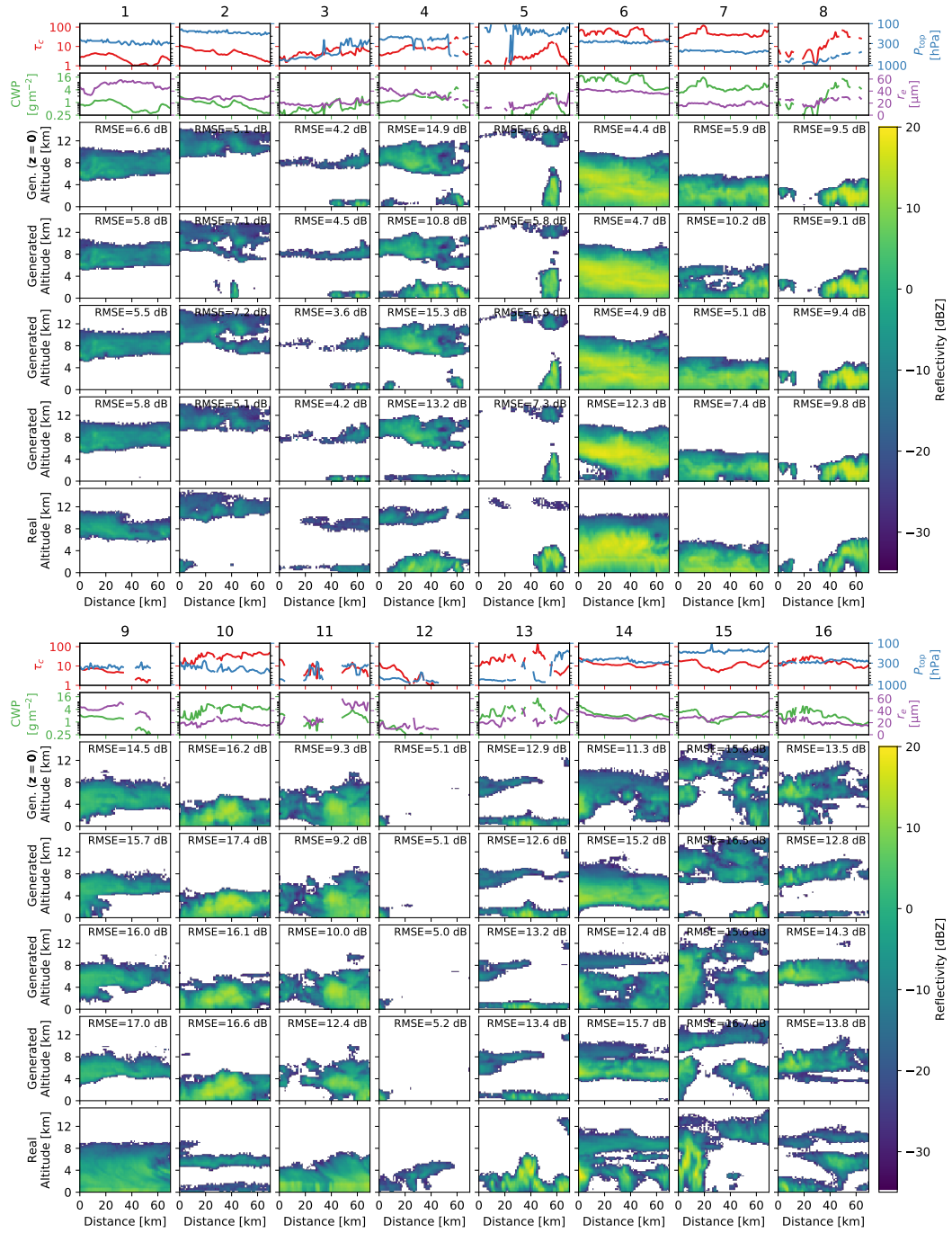


**Figure 1.** Examples of cloud scenes generated by the CGAN. Each of the 16 columns corresponds to one scene; the first two rows show the MODIS variables, the following four rows show examples of generated scenes (the first of these generated with zero noise), and the final row shows the real scene (i.e. the correct solution).

209 top height and the geometric thickness of the cloud are predicted to within 1 km, and  
 210 the radar reflectivity of the generated cloud also has very similar values. The textures  
 211 are also similar between the real and generated scenes: Scene 1 is relatively uniform, while  
 212 the structure of the cloud in scene 2 is more complex. However, the generator misses cer-  
 213 tain specific details in both scenes, such as the change in the altitude of the radar echo  
 214 top in the middle of scene 1, and the low-level cloud that is present in scene 2, although  
 215 in this case, one of the solutions does include a low-level cloud in the wrong position.

216 Columns 3–5 in Fig. 1 demonstrate various cases where the CGAN successfully in-  
 217 fers the presence of multilayer clouds. It appears that the generator exploits the spatial  
 218 variability of the MODIS variables to infer the presence of multiple cloud layers. In columns  
 219 3 and 4, the cloud top pressure  $P_{\text{top}}$  is variable, and this seems to drive the CGAN to  
 220 create multiple layers. In column 4, the best match to the real scene is notably not the  
 221 scene deemed most likely by the CGAN, but rather one of the randomly sampled scenes.  
 222 This demonstrates the advantage of the CGAN generating a distribution of possible pre-  
 223 dictions for a given input. In column 5, the increase of  $\tau_c$  and CWP on the right side  
 224 of the scene apparently allows the CGAN to infer the presence of a thick low-level cloud,  
 225 probably of convective origin, underlying the thinner cloud layer around 12 km altitude.

226 Columns 6–7 of Fig. 1 show high-reflectivity scenes where the radar echo reaches  
 227 the surface. In these scenes, as with columns 1–2, the cloud top height is accurately pre-  
 228 dicted by the GAN, as is the general intensity of the radar echo. The generated scenes  
 229 in column 6 also include traces of the melting layer bright band that is evident in the  
 230 real scene, although the generated bright band is not nearly as sharp as that in the real  
 231 scene. This could possibly be improved by including information about the atmospheric  
 232 temperature in the CGAN inputs, but we did not explore this in the current study. In  
 233 both columns 6 and 7, the most likely solution resembles the real scene quite closely, while  
 234 the randomly sampled scenes include some solutions where the radar echo does not reach  
 235 the surface, leading to a higher RMSE.

236 Finally, column 8 of Fig. 1 demonstrates a case where gaps in cloud detection by  
 237 CloudSat are correctly predicted by the CGAN; while there are gaps in the MODIS data,  
 238 these clearly do not correspond exactly to the missing CloudSat echoes. This demon-  
 239 strates that the CGAN can predict situations where CloudSat would not detect a cloud  
 240 even though it is seen by MODIS. Conversely, there are significant MODIS data gaps  
 241 on the right side of the scene, but the CGAN correctly generates a low-level cloud there  
 242 regardless; apparently the CGAN can recognize situations where data gaps are caused  
 243 by missing data (for example, rejected retrievals) rather than actual absence of clouds,  
 244 and enforce continuity in the generated cloud scene.

245 Unlike scenes 1–8, in scenes 9–16 of Fig. 1 the CGAN has some difficulty making  
 246 the correct prediction. In column 9, the radar echo in the real scene reaches the ground,  
 247 while the generated scenes do not reproduce this. In scene 10, a multilayer cloud is in-  
 248 correctly interpreted as a deeper, single-layer cloud. The real scene in column 11 is quite  
 249 uniform and contains a pronounced reflectivity intensification at the melting layer; in the  
 250 generated scenes, the layer is much thinner on the left side of the scene than on the right,  
 251 and no melting layer is present. Notably, the MODIS data in this scene contain rather  
 252 large gaps that have no obvious counterpart in the CloudSat data. In column 12, the real  
 253 scene contains a detected cloud that covers almost all of the horizontal extent of the scene,  
 254 but the CGAN predicts a radar echo much more concentrated on the left side. In the  
 255 scene shown in column 13, the CGAN generates a spurious second cloud layer on the left  
 256 and the center, and also mostly misses the convective cloud in the middle of the scene.  
 257 Finally, columns 14–16 contain complicated scenes that the CGAN appears to find dif-  
 258 ficult to interpret. In each case, there is considerable variability among the generated  
 259 scenes, none of which correspond to the real scene particularly well. The common fea-  
 260 ture in these scenes seems to be that a high, continuous cloud layer masks MODIS from  
 261 seeing the cloud layers below. In such cases, it is hardly surprising that not much can

262 be reliably predicted about the underlying clouds. Thus, the high variability among the  
 263 generated radar reflectivity fields seems to reflect the uncertainty of the CGAN about  
 264 the correct solution.

265 Naturally, in probabilistic predictions, the most likely solution is not always the  
 266 correct one; rather, in a properly functioning probabilistic model, one would expect to  
 267 find the correct solution somewhere within the predicted distribution. In Fig. 1, only four  
 268 generated solutions are shown for each case due to space constraints. Such few samples  
 269 cannot be expected to completely represent the entire probability space. In order to fur-  
 270 ther explore the probability space of our predictions, we have included Figs. S2–S9 in  
 271 the supplement. These correspond to each of the problematic scenes 9–16 of Fig. 1, but  
 272 show 64 randomly generated examples for each scene. Additionally, to widen the range  
 273 of predictions made by the CGAN, we used a noise standard deviation of 2 rather than  
 274 1 in the noise input  $\mathbf{z}$  of the generator. As expected, increasing the noise standard de-  
 275 viation led to a higher variability in the generated scenes. Meanwhile, this increase in  
 276 the noise did neither reduce the credibility of the generated images, nor trigger the gen-  
 277 eration of obvious artifacts.

278 With the higher variability and the larger number of generated samples drawn for  
 279 each scene, the generated probability space in most cases includes scenes that correspond  
 280 closely to the correct solution. Solutions where the reflectivity field reaches the surface  
 281 can be found for scene 9 (Fig. S2), and multiple cloud layers at roughly the right alti-  
 282 tudes are present in some examples in scene 10 (Fig. S3), although the radar reflectiv-  
 283 ity in these remains too high. Likewise, some solutions in Fig. S4 are considerably more  
 284 horizontally uniform than those found in scene 11 of Fig. 1, and the solutions in Fig. S5  
 285 include scenes with extended low level clouds resembling that of the real solution in col-  
 286 umn 12. In Fig. S6, there are some solutions where the spurious cloud on the left is weaker  
 287 than in the solutions shown in column 13, and others where the convective cloud in the  
 288 middle is stronger. These solutions improve the representation of these features, but none  
 289 of the generated scenes in Fig. S6 completely reproduce the real scene; in particular, the  
 290 spurious second cloud layer persists at least partially in all of the generated images. In  
 291 Figs. S7–S9, corresponding to columns 14–16 of Fig. 1, the high variability of the gen-  
 292 erated scenes further demonstrates the uncertainty of the CGAN about the vertical struc-  
 293 ture of the clouds. This is accompanied by a higher RMS variability, indicated on top  
 294 of each plot, which can be used as a simple diagnostic for uncertainty about the correct  
 295 solution. In each of these cases, some of the generated images somewhat resemble the  
 296 real scene, indicating that the highly variable solution space also includes the correct so-  
 297 lution with a non-negligible probability.

298 The scenes shown in Fig. 1 were selected manually to demonstrate the operation  
 299 of our CGAN in various situations. As such, they are not statistically representative of  
 300 the dataset. In order to provide further examples of the functionality of the CGAN over  
 301 the entire dataset, we have also included Figs. S10–S17 in the supplementary material.  
 302 These figures are equivalent to Figs. 1, except that the cases shown in them have been  
 303 selected randomly.

## 304 4.2 Dependence on MODIS parameters

305 The above analysis suggests that the CGAN has learned a fairly complex, nonlin-  
 306 ear response to the MODIS variables. Nevertheless, it can be instructive to examine how  
 307 the generator responds to simple changes in the input variables. In Fig. 2, we have plot-  
 308 ted the changes in the generated cloud scene while varying each of the four MODIS vari-  
 309 ables individually. The middle column shows the scene generated from synthetic MODIS  
 310 data with all transformed variables (as defined in Eqs. 2–5) set to their mean values in  
 311 the dataset, while each row shows the variability of the generated scene when a single  
 312 input variable is varied from 2 standard deviations below the mean ( $-2.0\sigma$ ) to 2 stan-



313

dard deviations above the mean ( $+2.0\sigma$ ). All scenes have been generated with zero noise in order to give the most likely answer according to the generator.

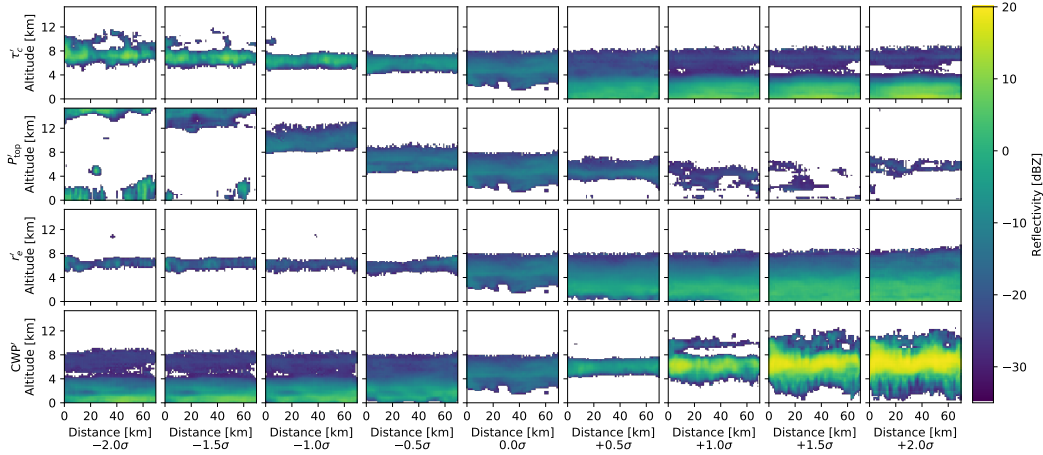


**Figure 2.** The response of the generator to changes in the input variables. The middle column shows the generated scene with all variables set to their mean values. Each row shows the response to changes a single variable ranging from  $-2$  to  $+2$  standard deviations.

314

315

316

317

318

319

320

321

322

323

324

325

326

327

In many cases, the scenes generated in this way do not look physically realistic. This is probably because, in reality, the parameters do not vary individually, but are significantly correlated. Nevertheless, it is encouraging the generator is well behaved in the sense that no scenes contain obvious image processing artifacts, and the response to the parameters is smooth. The response to the change in  $P_{\text{top}}$  is the easiest to interpret, as increasing  $P_{\text{top}}$  corresponds to lowering echo tops in the generated cloud scene up to  $+1\sigma$ . This good correspondence can be expected, as the CGAN also accurately predicted the echo top heights in Sect. 4.1. However, at high  $P_{\text{top}}$ , the clouds become increasingly thin and multilayered. The low cloud layer, which seems to correspond to the  $P_{\text{top}}$  observation, is barely visible at  $+1.5\sigma$  and disappears altogether at  $+2.0\sigma$ . The lowest- $P_{\text{top}}$  scenes are also accompanied by lower-altitude clouds. A plausible explanation of this is that very low  $P_{\text{top}}$  usually occurs with anvil clouds originating from deep convection, which is often accompanied by shallower convective clouds.

328

329

330

331

332

333

334

The effective radius  $r_e$  is another variable for which one can make a physical interpretation of the generator response. In this case, low  $r_e$  occurs in nature in non-precipitating clouds, which tend to be somewhat shallow in vertical extent, and also have weak radar reflectivity signatures. Conversely, high  $r_e$  typically occurs in precipitating clouds, which have higher reflectivities that cover a larger vertical extent (as the radar is sensitive to the precipitation in addition to the cloud). The CGAN response to  $r_e$  is consistent with this relationship.

335

336

337

338

339

340

341

342

343

The effects of  $\tau_c$  and  $CWP$  individually are difficult to interpret, since in practice, these two variables are strongly dependent on each other (for details, see, e.g. Grosvenor et al., 2018). Thus, it is physically unrealistic to change one of these without changing the other. Low values of  $\tau_c$  create a vertically shallow, high-reflectivity cloud layer, which probably would not occur in realistic scenarios. Meanwhile, high values of  $\tau_c$  create a deep, high-reflectivity (i.e. precipitating) region with a low-reflectivity layer on top. Curiously, the scenes generated with low  $CWP$  are similar to those produced by high  $\tau_c$ . Meanwhile, high  $CWP$  leads to a rather unrealistic-looking layer with high reflectivity around 5–8 km altitude, with lower-reflectivity regions both above and below.

344

### 4.3 Cloud vertical distribution

345

346

347

348

349

350

351

352

353

A downside of using adversarial training in GANs is that there is not a clear, specific metric to judge model performance. However, we can still examine the distribution of data statistically and compare between the generated and real datasets. A commonly used method for analysing radar data climatologically is to present the aggregated data as a two-dimensional joint distribution of altitude and radar reflectivity, sometimes called contour frequency by altitude diagram (CFAD; e.g. Steiner, Houze, & Yuter, 1995). We present these distributions for our dataset in Fig. 3. The histogram for the real data was computed from the validation dataset, while the generated histogram was obtained by running the generator for each scene in the validation set using randomly sampled noise.

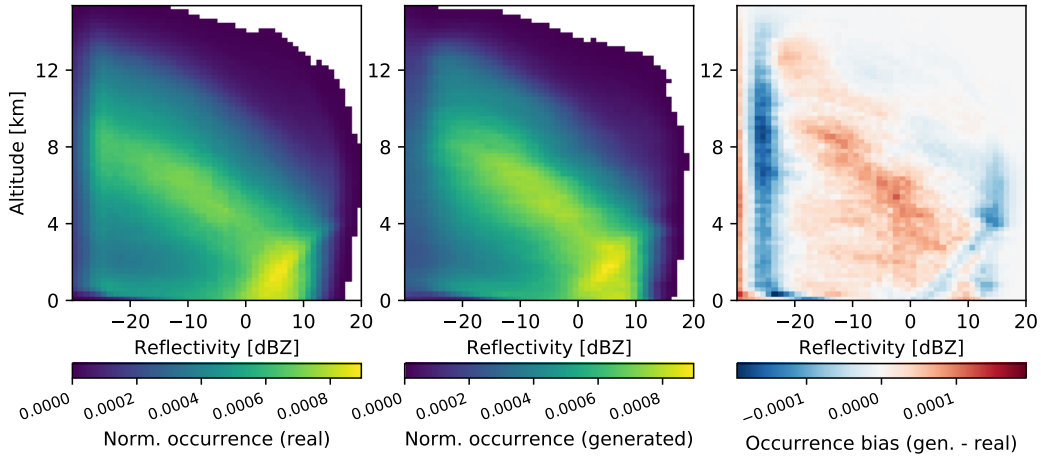


**Figure 3.** Normalized reflectivity–altitude histograms. Left: from the real dataset. Middle: from the generated dataset. Right: the difference of the middle and left panels.

354

355

356

357

358

359

360

361

Clearly, the generated histogram replicates the most significant features of the histogram for the real dataset. The CGAN also replicates the decreasing occurrence near  $-30$  dBZ reflectivity, which is caused by the CloudSat radar detecting only some of the radar echoes near its sensitivity limit. However, this transition appears to be more gradual in the generated data than in the real dataset. The extremes of the real and generated histograms also seem to have similar distributions, indicating that the CGAN captures the data distribution well near the extreme values.

362

363

364

365

366

367

368

The relationship of reflectivity and altitude can also help illustrate regional difference in cloud structure (Leinonen, Lebsock, Oreopoulos, & Cho, 2016; Oreopoulos, Cho, & Lee, 2017). In Figs. S18–S24 of the supplementary material, we also show the same plot along  $20^\circ$  zonal bands. The accuracy of these is similar to Fig. 3, indicating that the GAN does not suffer from significant regional bias. Furthermore, we show the standard deviation of occurrence for both the real and generated data in Fig. S25, which indicates that the generator correctly captures the variability of the data.

369

## 5 Conclusions

370

371

372

The CGAN described in this study is capable of generating crisp images that strongly resemble the radar reflectivity scenes in the dataset. Most of the time, the CGAN generates cloud vertical structures that are close to those measured by CloudSat, using only

373 the collocated MODIS data as input. The generator is capable of exploiting the spatial  
 374 structure of information in the input data, most notably inferring the presence of mul-  
 375 tilayer clouds. It is robust in cases of missing data, being able to interpolate into regions  
 376 of missing MODIS inputs. The generator can also characterize the uncertainty of its pre-  
 377 dictions to some degree, creating more variability in its outputs in cases where the un-  
 378 certainty is high, although we observed a few cases where the variability appears under-  
 379 estimated, as none of the generated scenes in the output distribution match the real scene  
 380 particularly well. The generator is also able to generalize its learning to the validation  
 381 dataset, which was not used for training.

382 Based on these results, we argue that machine learning using GANs (and CGANs  
 383 specifically) has potential to solve a variety of problems in atmospheric remote sensing,  
 384 and observational Earth science in general. Typical problems in this field of study in-  
 385 volve complex spatial structures, which CNNs handle effectively, and incomplete mea-  
 386 surements, which are best treated using probability distributions, an integral feature of  
 387 GANs. Conditional probability problems, in particular, are ubiquitous in the formula-  
 388 tion of remote sensing retrieval problems, and are naturally handled by CGANs. This  
 389 study is intended to demonstrate these capabilities and lay the foundations for further  
 390 investigations that target more practical applications. For instance, reconstructing 3D  
 391 cloud scenes from MODIS 2D imagery, as opposed to reconstructing 2D vertical profiles  
 392 from 1D MODIS data in this study, would make available an estimate of cloud vertical  
 393 structure over very large areas, as the MODIS data cover a swath of over 2000 km rather  
 394 than the single nadir-pointing scan obtained by CloudSat. This could also be useful in  
 395 the context of missions such as EarthCARE, for which 3D reconstruction algorithms are  
 396 being developed (Barker et al., 2011). Implementing such reconstruction using GANs  
 397 will likely involve substantial challenges related to network design and computational re-  
 398 quirements.

399 Further research is also needed to ensure the physical realism of machine-learning  
 400 models. In the current study, the generator does not perform any explicit physical sim-  
 401 ulation of clouds, which limits its ability to generalize on its training, and may produce  
 402 biases for inputs that are not within the training data distribution. We recommend that  
 403 future studies investigate combining the capabilities of GANs with the constraints pro-  
 404 vided by physics-based simulations of clouds.

## 405 Acknowledgments

406 The original CloudSat data products 2B-GEOPROF and MOD06-AUX are available at  
 407 the CloudSat Data Processing Center, <http://www.cloudsat.cira.colostate.edu/>.  
 408 The training dataset has been made available by Leinonen (2019). A Python/Keras im-  
 409 plementation code that can be used to reproduce the results is available at [https://github](https://github.com/jleinonen/cloudsat-gan)  
 410 [.com/jleinonen/cloudsat-gan](https://github.com/jleinonen/cloudsat-gan).

411 The research of JL and AG was carried out at the Jet Propulsion Laboratory (JPL),  
 412 California Institute of Technology, under a contract with the National Aeronautics and  
 413 Space Administration (NASA) and funded through the internal Research and Technol-  
 414 ogy Development program. The High Performance Computing resources used in this in-  
 415 vestigation were provided by funding from the JPL Office of the Chief Information Of-  
 416 ficer. TY acknowledges funding from NASA Grant 80NSSC18M0084, “Making Earth Sys-  
 417 tem Data Records for Use in Research Environments”, PM: Lucia Tsaoussi.

## 418 References

419 Barker, H. W., Jerg, M. P., Wehr, T., Kato, S., Donovan, D. P., & Hogan, R. J.  
 420 (2011). A 3D cloud-construction algorithm for the EarthCARE satellite mis-  
 421 sion. *Quart. J. Roy. Meteor. Soc.*, 137(657), 1042–1058. doi: 10.1002/qj.824

- 422 Borji, A. (2018). Pros and cons of GAN evaluation measures. *arXiv preprint*  
 423 *arXiv:1802.03446*. Retrieved from <https://arxiv.org/abs/1802.03446>
- 424 Garay, M. J., de Szoeke, S. P., & Moroney, C. M. (2008). Comparison of marine  
 425 stratocumulus cloud top heights in the southeastern Pacific retrieved from  
 426 satellites with coincident ship-based observations. *J. Geophys. Res. Atmos.*,  
 427 *113*, D18204. doi: 10.1029/2008JD009975
- 428 Goodfellow, I., Pouget-Abadie, J., Mirza, M., Xu, B., Warde-Farley, D., Ozair,  
 429 S., ... Bengio, Y. (2014). Generative adversarial nets. In Z. Ghahra-  
 430 mani, M. Welling, C. Cortes, N. D. Lawrence, & K. Q. Weinberger (Eds.),  
 431 *Advances in Neural Information Processing Systems 27* (pp. 2672–2680).  
 432 Curran Associates, Inc. Retrieved from [http://papers.nips.cc/paper/](http://papers.nips.cc/paper/5423-generative-adversarial-nets.pdf)  
 433 [5423-generative-adversarial-nets.pdf](http://papers.nips.cc/paper/5423-generative-adversarial-nets.pdf)
- 434 Grosvenor, D. P., Sourdeval, O., Zuidema, P., Ackerman, A., Alexandrov, M. D.,  
 435 Bennartz, R., ... Quaas, J. (2018). Remote sensing of droplet number con-  
 436 centration in warm clouds: A review of the current state of knowledge and  
 437 perspectives. *Rev. Geophys.*, *56*(2), 409–453. doi: 10.1029/2017RG000593
- 438 Guillaume, A., Kahn, B. H., Yue, Q., Fetzer, E. J., Wong, S., Manipon, H., G.  
 439 J. Hua, & Wilson, B. D. (2018). Horizontal and vertical scaling of cloud  
 440 geometry inferred from CloudSat data. *J. Atmos. Sci.*, *75*, 2187–2197. doi:  
 441 [10.1175/JAS-D-17-0111.1](https://doi.org/10.1175/JAS-D-17-0111.1)
- 442 Ham, S.-H., Kato, S., Barker, H. W., Rose, F. G., & Sun-Mack, S. (2015). Im-  
 443 proving the modelling of short-wave radiation through the use of a 3D scene  
 444 construction algorithm. *Quart. J. Roy. Meteor. Soc.*, *141*(690), 1870–1883. doi:  
 445 [10.1002/qj.2491](https://doi.org/10.1002/qj.2491)
- 446 Ioffe, S., & Szegedy, C. (2015). Batch normalization: Accelerating deep network  
 447 training by reducing internal covariate shift. *arXiv preprint arXiv:1502.03167*.  
 448 Retrieved from <https://arxiv.org/abs/1511.06434>
- 449 Kingma, D. P., & Ba, J. (2014). Adam: A method for stochastic optimization. In  
 450 *3rd International Conference for Learning Representations, San Diego, Califor-*  
 451 *nia, USA*. Retrieved from <https://arxiv.org/abs/1412.6980>
- 452 Krizhevsky, A., Sutskever, I., & Hinton, G. E. (2012). ImageNet classification  
 453 with deep convolutional neural networks. In F. Pereira, C. J. C. Burges,  
 454 L. Bottou, & K. Q. Weinberger (Eds.), *Advances in Neural Information Pro-*  
 455 *cessing Systems 25* (pp. 1097–1105). Curran Associates, Inc. Retrieved from  
 456 [http://papers.nips.cc/paper/4824-](http://papers.nips.cc/paper/4824-imagenet-classification-with-deep-convolutional-neural-networks.pdf)  
 457 [convolutional-neural-networks.pdf](http://papers.nips.cc/paper/4824-imagenet-classification-with-deep-convolutional-neural-networks.pdf)
- 458 LeCun, Y., Bengio, Y., & Hinton, G. (2015). Deep learning. *Nature*, *521*, 436–444.  
 459 doi: [doi.org/10.1038/nature14539](https://doi.org/10.1038/nature14539)
- 460 Leinonen, J. (2019). *Replication data for: Reconstruction of cloud vertical struc-*  
 461 *ture with a generative adversarial network*. Harvard Dataverse. Retrieved from  
 462 <https://doi.org/10.7910/DVN/BZEZC2> doi: 10.7910/DVN/BZEZC2
- 463 Leinonen, J., Lebsock, M. D., Oreopoulos, L., & Cho, N. (2016). Interregional dif-  
 464 ferences in MODIS-derived cloud regimes. *J. Geophys. Res. Atmos.*, *121*(19),  
 465 11648–11665. doi: 10.1002/2016JD025193
- 466 Marchand, R., Ackerman, T., Smyth, M., & Rossow, W. B. (2010). A review  
 467 of cloud top height and optical depth histograms from MISR, ISCCP, and  
 468 MODIS. *J. Geophys. Res. Atmos.*, *115*, D16206. doi: 10.1029/2009JD013422
- 469 Marchand, R., Mace, G. G., Ackerman, T., & Stephens, G. (2008). Hydrometeor  
 470 detection using *Cloudsat* — an Earth-orbiting 94-GHz cloud radar. *J. Atmos.*  
 471 *Oceanic Technol.*, *25*, 519–533. doi: 10.1175/2007JTECHA1006.1
- 472 Mirza, M., & Osindero, S. (2014). Conditional generative adversarial nets.  
 473 *arXiv preprint arXiv:1411.1784*. Retrieved from [https://arxiv.org/abs/](https://arxiv.org/abs/1411.1784)  
 474 [1411.1784](https://arxiv.org/abs/1411.1784)
- 475 Nair, V., & Hinton, G. E. (2010). Rectified linear units improve restricted Boltz-  
 476 mann machines. In *Proceedings of the 27th international conference on ma-*

- 477 *chine learning* (pp. 807–814).
- 478 Oreopoulos, L., Cho, N., & Lee, D. (2017). New insights about cloud vertical struc-  
479 ture from CloudSat and CALIPSO observations. *J. Geophys. Res. Atmos.*,  
480 *122*(17), 9280–9300. doi: 10.1002/2017JD026629
- 481 Platnick, S., King, M. D., Ackerman, S. A., Menzel, W. P., Baum, B. A., Riedi,  
482 J. C., & Frey, R. A. (2003). The MODIS cloud products: algorithms and  
483 examples from Terra. *IEEE Trans. Geosci. Remote Sens.*, *41*(2), 459–473. doi:  
484 10.1109/TGRS.2002.808301
- 485 Radford, A., Metz, L., & Chintala, S. (2015). Unsupervised representation learning  
486 with deep convolutional generative adversarial networks. In *4rd International  
487 Conference for Learning Representations, San Juan, Puerto Rico, USA*. Re-  
488 trieved from <https://arxiv.org/abs/1511.06434>
- 489 Steiner, M., Houze, R. A., & Yuter, S. E. (1995). Climatological characterization of  
490 three-dimensional storm structure from operational radar and rain gauge data.  
491 *J. Appl. Meteor.*, *34*(9), 1978–2007. doi: 10.1175/1520-0450(1995)034<1978:  
492 CCOTDS>2.0.CO;2
- 493 Stephens, G. L. (2005). Cloud feedbacks in the climate system: A critical review. *J.*  
494 *Clim.*, *18*(2), 237–273. doi: 10.1175/JCLI-3243.1
- 495 Stephens, G. L., Vane, D. G., Tanelli, S., Im, E., Durden, S., Rokey, M., ... Marc-  
496 hand, R. (2008). CloudSat mission: Performance and early science after  
497 the first year of operation. *J. Geophys. Res. Atmos.*, *113*, D00A18. doi:  
498 10.1029/2008JD009982
- 499 Stevens, B., & Bony, S. (2013). What are climate models missing? *Science*,  
500 *340*(6136), 1053–1054. doi: 10.1126/science.1237554
- 501 Vial, J., Dufresne, J.-L., & Bony, S. (2013). On the interpretation of inter-model  
502 spread in CMIP5 climate sensitivity estimates. *Clim. Dynam.*, *41*(11), 3339–  
503 3362. doi: 10.1007/s00382-013-1725-9
- 504 Várnai, T., & Marshak, A. (2002). Observations of three-dimensional radiative ef-  
505 fects that influence MODIS cloud optical thickness retrievals. *J. Atmos. Sci.*,  
506 *59*(9), 1607–1618. doi: 10.1175/1520-0469(2002)059<1607:OOTDRE>2.0.CO;2